A&A 497, 41–51 (2009)
DOI: 10.1051/0004-6361/200810506

Astronomy & Astrophysics

Early-type galaxies in the near-infrared: 1.5–2.4 μm spectroscopy⋆,⋆⋆

M. Cesetti[1,2], V. D. Ivanov[1], L. Morelli[2], A. Pizzella[2], L. Buson[3], E. M. Corsini[2], E. Dalla Bontà[2], M. Stiavelli[4], and F. Bertola[2]

[1] European Southern Observatory, Ave. Alonso de Còrdova 3107, Casilla 19, Santiago 19001, Chile
e-mail: [mcesetti;vivanov]@eso.org
[2] Dipartimento di Astronomia, Università di Padova, vicolo dell'Osservatorio 3, 35122 Padova, Italy
e-mail: [mary.cesetti;lorenzo.morelli;alessandro.pizzella;enricomaria.corsini;elena.dallabonta;francesco.bertola]@unipd.it
[3] Istituto Nazionale di Astrofisica, Osservatorio Astronomico di Padova, Vicolo dell'Osservatorio 5, 35122 Padova, Italy
e-mail: lucio.buson@oapd.inaf.it
[4] Space Telescope Science Institute, 3700 San Martin Drive, Baltimore, MD 21218, USA
e-mail: mstiavel@stsci.edu

Received 2 July 2008 / Accepted 21 August 2008

ABSTRACT

Context. Near-infrared (hereafter NIR) data may provide complementary information to the traditional optical population synthesis analysis of unresolved stellar populations because the spectral energy distribution of the galaxies in the 1–2.5 μm range is dominated by different types of stars than at optical wavelengths. Furthermore, NIR data are less affected by dust absorption and hence could constrain the stellar populations in dust-obscured galaxies.
Aims. We attempt to develop observational constraints on the stellar populations of unresolved stellar systems in the NIR.
Methods. To achieve this goal, we require benchmark NIR spectra of "simple" early-type galaxies, to test and calibrate the outputs of population synthesis models. We obtained low-resolution ($R \sim 1000$) long-slit spectra between 1.5 and 2.4 μm for 14 nearby early-type galaxies using SofI at the ESO 3.5-m New Technology Telescope and higher resolution ($R \sim 3000$) long-slit spectra, centered on MgI at ~1.51 μm for a heterogeneous sample of 5 nearby galaxies observed with ISAAC at Antu, one of the 8.2-m ESO Very Large Telescope.
Results. We defined spectral indices corresponding to CO, NaI, CaI and MgI absorption lines and measured their strengths in the galaxies spectrum. We defined a new global NIR metallicity index, suitable for abundance measurements in low-resolution spectra. Finally, we created an average-combined NIR spectrum of an early-type galaxy, from a homogeneous subset of our data set.
Conclusions. The NIR galaxy spectra are similar to each other and some of the line index strengths correlate with both the iron abundance [Fe/H] and optical metal line indices of the galaxies. The data suggest that the NIR metal features, in combination with a hydrogen absorption feature, may break the age-metallicity degeneracy in a similar way the Mg and Fe features in the rest-frame optical wavelength range.

Key words. infrared: galaxies – Galaxy: abundances – galaxies: elliptical and lenticular, cD – galaxies: spiral – galaxies: stellar content

1. Introduction

State-of-the-art space-based instrumentation can resolve the stellar populations only of galaxies in the Local Group and in more distant objects we can usually detect only the tip of the red giant branch stars, which are rarely sufficient for robust population analyses. We must therefore infer the stellar population properties indirectly from the integrated galaxy light. The complex mix of stellar populations present in most galaxies imply that it is usually possible to study only the properties of the most recent generation of stars. However, properties such as stellar kinematics and present-day metal content are affected significantly by the overall star formation history and, due to the well known age-metallicity degeneracy (Faber 1973; O'Connell 1986; Worthey 1994), they often lead to non-unique solutions for the stellar populations. In this respect, the Lick/IDS system of indices pioneered by Burstein et al. (1984) and Faber et al. (1985), and developed further by Trager et al. (1998, 2000, 2005), has been particularly successful in interpreting the integrated optical light of galaxies.

However, new constraints are necessary to interpret more complicated systems and one possibility is to widen the spectral range towards the near-infrared (NIR) because light in different wavebands is dominated by different populations of stars. The NIR passbands are dominated by light from older and redder stars and therefore offer us the possibility to study other stellar populations than possible with optical spectra alone. In addition, abundance determinations with optical spectroscopy are impossible for heavily reddened evolved stellar populations such as dusty spheroids or some bulge globular clusters hidden by dust (e.g. Stephens & Frogel 2004). NIR spectroscopic observations could overcome these problems because the extinction in the K-band is only one-tenth that in the V-band.

⋆ Based on observations made with ESO Telescopes at the La Silla and Paranal Observatory under programmes 69.B-0311 and 077.B-0163.
⋆⋆ Full Table 5 is only available in electronic form at the CDS via anonymous ftp to cdsarc.u-strasbg.fr (130.79.128.5) or via http://cdsweb.u-strasbg.fr/cgi-bin/qcat?J/A+A/497/41

Most of the previous work at NIR was focused on either active galactic nuclei (AGNs) or objects with very strong star formation, including recent surveys of ultra-luminous infrared galaxies (Goldader et al. 1995; Murphy et al. 1999, 2001; Burston et al. 2001), luminous infrared galaxies (Goldader et al. 1997; Reunanen et al. 2007), starbursts (Engelbracht 1997; Coziol et al. 2001), Seyfert galaxies (Ivanov et al. 2000; Sosa-Brito et al. 2001; Reunanen et al. 2002; Boisson et al. 2002), LINERs (Larkin et al. 1998; Alonso-Herrero et al. 2000; Sosa-Brito et al. 2001), and interacting galaxies (Vanzi & Rieke 1997; Vanzi et al. 1998).

Relatively few NIR spectroscopic observations exist for "normal" galaxies. Only Mannucci et al. (2001) provided low-resolution ($R \sim 400$) template spectra for galaxies of different Hubble types, including some giant ellipticals. Such data, together with the corresponding analysis is a necessary first step towards developing a system of spectral diagnostics in the NIR because well-understood galaxies with relatively simple star-forming histories allow us to tune the NIR population synthesis models. Silva et al. (2008, hereafter S08) studied the stellar populations of eleven early-type galaxies in the nearby Fornax cluster by means of K-band spectroscopy.

A few prominent NIR features were first studied by Origlia et al. (1993), who demonstrated that they represent a superb set of indicators for constraining the average spectral type and luminosity class of cool, evolved stars. This conclusion was later confirmed by Förster Schreiber (2000) and Ivanov et al. (2004). Furthermore, the same NIR features appear to be promising abundance indicators (Frogel et al. 2001; Stephens & Frogel 2004).

Here we describe two new data sets of high quality NIR spectra of ellipticals/spirals designed to provide a benchmark for future NIR studies of unresolved galaxies: (i) low-resolution spectra covering the range from 1.5 to 2.4 μm that include strong features such as CO, NaI and CaI that are traditionally studied, and (ii) moderate resolution spectra around the MgI absorption feature at 1.51 μm. This is the second strongest Mg feature in the H- and K-band atmospheric windows (after the feature at 1.71 μm) and at zero redshift is located in a region of poor atmospheric transmission, making it difficult to observe in stars. However, at high redshift the observable rest-frame spectrum of external galaxies increases to wavelengths at which the atmosphere is more transparent (Ivanov 2001), close to the 1.71 μm MgI, which itself becomes affected by the red edge of the H-band atmospheric window.

We are only few years from the launch of the James Webb Space Telescope (Gardner et al. 2006), a space-based infrared telescope that will have unprecedented capabilities. Therefore, in the near future the application of NIR spectroscopy to the study of galaxy properties will be limited not by lack of data but by our understanding of spectral features at these wavelengths. Improving the characterization of the NIR indices is a timely step in this direction.

The paper is organized as follows. The sample selection is discussed in Sect. 2. The NIR spectroscopic observations and data reduction are described in Sect. 3. The definition of the new NIR spectral indices and their measurements are given in Sect. 4. Results are discussed in Sect. 5 and summarized in Sect. 6.

2. The sample

Our main sample consists of 14 nearby bright ($B_T \leq 14.1$ mag), undisturbed spheroids. They were selected to cover a wide range of luminosity and velocity dispersion and to have Lick/IDS line-strength indices available, from the literature. Six of our galaxies are giant ellipticals (NGC 4472, NGC 4621, NGC 4649, NGC 4697, NGC 6909, IC 4296), five are intermediate-size ellipticals (NGC 4478, NGC 4564, NGC 3818, NGC 5077, NGC 5576), one is a bright dwarf elliptical (NGC 3641), and two are bulges of disk galaxies (NGC 4281, NGC 4594; our spectra are dominated by their spheroids). The Mg_2 index spans the range between 0.21 and 0.34 mag (Bender et al. 1993), in agreement with other Mg_2 literature values, and the central velocity dispersions are between about 130 and 370 km s^{-1}. The galaxy properties are summarized in Table 1.

Four galaxies in the sample exhibit evidence for weak nuclear activity: NGC 4594 and NGC 5077 were identified as LINERs by Heckman (1980); NGC 4472 is a weak Seyfert 2 (Ho et al. 1997); and IC 4296 shows radio and X-ray emission (Rinn et al. 2005). Finally, NGC 4649 is a close companion of the giant spiral NGC 4647 and it may have undergone some tidal stripping (Das & Jog 1999).

The low resolution used for the observation of our sample is insufficient to characterize the 1.51 μm MgI feature, so we selected higher resolution spectra from the ESO Science Archive, covering the region around the 1.51 μm, for a heterogeneous set of galaxies. Although these observations were acquired for other purposes, they provide a first glimpse into the behavior of this feature. The properties of these galaxies are also described in Table 1.

3. Observation and data reduction

3.1. SofI low-resolution spectra

Long-slit ($0\farcs6 \times 290''$) NIR spectroscopy of 14 galaxies was performed with the SofI (Son of ISAAC) infrared spectrometer (Moorwood et al. 1998b) at the Nasmyth A focus of the ESO 3.5-m New Technology Telescope (NTT) at the European Southern Observatory (ESO) in la Silla (Chile). The detector is a 1024×1024 pixels Hawaii HgCdTe array with a 18.5-μm pixel size. It is read out in four quadrants and the average quantum efficiency is ~65 %. We used the low resolution grism ($R \sim 1000$) which provided a spectral dispersion of 10.22 Å pixel^{-1} and a coverage of between 1.53 μm and 2.52 μm.

The smaller galaxies were observed in nodding mode, placing them at two different positions along the slit, separated by $150''$. In the case of larger galaxies, the telescope pointing was alternated between the galaxy and a nearby clear sky region to obtain a good sky sampling. We randomly dithered the telescope within a $10''$ box along the slit about each position. This dithering, also known as jitter (see e.g. SofI handbook or Devillard 1999), helped us to eliminate bad pixel events, and to improve both the pixel sampling and flat-field correction, because, on each image, the object was placed on slightly different positions of the array.

Immediately before or after each galaxy spectrum we observed a B star to measure the atmospheric transmission and the instrument response, always in nodding mode and with a similar airmass to that of the corresponding galaxy. Finally, to calibrate the spatial distortions we also obtained a sequence of stellar spectra placed at 19 equidistant positions along the slit.

The details of the spectroscopic observations are given in Table 2.

Table 1. Basic properties of the sample galaxies.

ID	Galaxy	RA(2000)	Dec (2000)	Type	Redshift	σ	B_T	H_T	K_T	Age	Mg_2	Mg_2	H_β	Fe5335	[Z/H]	[Fe/H]	CaT
						(km s^{-1})	(mag)	(mag)	(mag)	(Gyr)	(mag)	(mag)	(Å)	(Å)	(Å)	(Å)	(Å)
(1)	(2)	(3)	(4)	(5)	(6)	(7)	(8)	(9)	(10)	(11)	(12a)	(12b)	(13)	(14)	(15)	(16)	(17)
Galaxies with low-resolution spectra																	
1	IC 4296	13 36 38.85	−33 57 59.3	E	0.0124(a)	337.0(a)	11.61	14.56	14.30	5.2(j)	0.323	0.340(a)	1.22(m)	3.03(m)	0.39(j)	…	…
2	NGC 3641	11 21 08.85	+03 11 40.2	E pec	0.0058(b)	163.2(i)	14.10	15.92	15.17	6.6(k)	0.284	0.273(k)	0.72(k)	2.39(k)	…	…	6.343
3	NGC 3818	11 41 57.50	−06 09 20.0	E5	0.0055(a)	187.5(a)	12.67	14.69	14.54	6.4(k)	0.315	0.322(a)	1.67(k)	2.87(k)	0.37(o)	0.16(o)	6.242
4	NGC 4281	12 20 21.52	+05 23 12.4	S0$^+$: sp	0.0089(c)	230.5(h)	12.25	13.91	13.80	…	0.314	…	…	…	…	…	…
5	NGC 4472	12 29 46.76	+07 59 59.9	E2	0.0033(a)	309.7(a)	9.37	15.34	15.01	10.0(k)	0.306	0.331(a)	1.37(k)	3.11(k)	0.26(o)	0.06(o)	6.119
6	NGC 4478	12 30 17.53	+12 19 40.3	E2	0.0047(a)	153.0(a)	12.36	15.62	15.45	6.9(k)	0.253	0.260(a)	1.67(k)	2.81(k)	0.30(o)	0.16(o)	6.810
7	NGC 4564	12 36 27.01	+11 26 18.8	E	0.0038(a)	171.1(a)	12.05	14.74	14.66	8.3(k)	0.321	0.329(a)	1.54(k)	2.81(k)	…	…	6.325
8	NGC 4594	12 39 59.43	−11 37 22.9	Sa(s) sp	0.0034(a)	259.1(a)	8.98	12.22	12.22	9.5(k)	0.330	0.338(a)	1.44(k)	…	…	0.39(o)	6.361
9	NGC 4621	12 42 02.39	+11 38 45.1	E5	0.0014(a)	232.0(a)	10.57	10.28	10.16	9.1(k)	0.328	0.345(a)	1.39(k)	2.98(k)	0.07(o)	…	6.055
10	NGC 4649	12 43 40.19	+11 33 08.9	E2	0.0036(a)	368.5(a)	9.81	14.61	14.35	11.9(m)	0.338	0.347(a)	1.29(k)	2.57(k)	0.29(o)	0.06(o)	…
11	NGC 4697	12 48 35.70	−05 48 03.0	E6	0.0041(a)	171.7(a)	10.14	13.35	13.31	6.4(k)	0.297	0.296(a)	1.69(k)	1.94(k)	0.06(o)	−0.03(o)	6.185
12	NGC 5077	13 19 31.66	−12 39 25.0	E3-4	0.0090(d)	255.9(i)	12.38	16.21	14.93	15.0(j)	0.295	0.324(j)	1.83(m)	2.64(m)	0.12(j)	…	…
13	NGC 5576	14 21 03.60	+03 16 14.4	E3	0.0050(e)	183.1(i)	11.85	14.94	14.74	…	0.253	0.243(f)	1.52(n)	3.11(l)	…	0.02(o)	…
14	NGC 6909	20 27 38.60	−47 01 34.0	E+:	0.0090(f)	128.7(f)	12.61	14.25	14.32	…	0.208	0.214(f)	2.17(p)	2.32(p)	…	…	…
Galaxies with high-resolution spectra																	
15	Mrk 1055	02 48 18.55	−08 57 37.4	S?	0.0366(v)	…	…	14.69	14.30	…	…	…	…	…	…	…	…
16	NGC 1144	02 55 12.32	−00 11 01.7	E	0.0288(q)	…	13.78	15.18	15.06	…	…	…	…	…	…	…	…
17	NGC 1362	03 33 53.08	−20 16 57.7	S0^o: pec	0.0041(t)	91(s)	…	16.11	15.68	…	…	…	0.223(f)	…	…	…	…
18	NGC 4472								see above								
19	NGC 7714	23 36 14.28	+02 09 17.8	Sb(s): pec	0.0093(p)	62(u)	13.00	15.85	16.08	…	…	…	…	…	…	…	4.7(u)

Columns: (1) Identification number, used in the plots, (2) Galaxy name, (3)–(4) coordinates, (5) morphological type from de Vaucouleurs et al. (1991, hereafter RC3), except for Mrk 1055 and NGC 1144 from the Lyon Extragalactic Database (LEDA), (6) redshift, (7) central velocity dispersion, (8) total observed blue magnitude from RC3, (9)–(10) total observed H and K magnitude from Cutri et al. (2003, 2MASS All-Sky Catalog of point sources), (11) age, (12)–(17) optical indices available in literature, (12a) the Mg_2 values from Bender et al. (1993) and (17) calcium Triplet from Cenarro et al. (2003).

References: (a) Smith et al. (2000), (b) Falco et al. (1999), (c) Binggeli et al. (1985), (d) da Costa et al. (1998), (e) Denicoló et al. (2005), (f) Wegner et al. (2003), (g) Kobayashi & Arimoto (1999), (h) Dalle Ore et al. (1991), (i) Faber et al. (1999), (j) Annibali et al. (2007), (k) Sánchez-Blázquez et al. (2007), (l) Howell (2005), (m) Rampazzo et al. (2005), (n) Trager et al. (1998), (o) Trager et al. (2000), (p) Ogando et al. (2008), (q) Keel (1996), (r) Lauberts & Valentijn (1989), (s) Bernardi et al. (2002), (t) Oliva et al. (1995), (u) Gardner et al. (2006), (v) Lu et al. (1993).

Table 2. Log of the spectroscopic observations.

ID	Galaxy	Obs. Date YYYY-MM-DD	Exp. Time (s)	Slit PA (deg)	Galaxy sec z	Standard Star Sp.Type	Standard Star sec z	Aper-ture (arcsec)	*S/N*
(1)	(2)	(3)	(4)	(5)	(6)	(7)	(8)	(9)	(10)
Galaxies with low-resolution spectra									
1	IC 4296	2006-04-17	1200	0.0	1.19	B2V	1.19	6.8	85.5
2	NGC 3641	2006-04-17	3600	70.0	1.20	B2V	1.21	4.0	60.2
3	NGC 3818	2006-04-17	3600	100.0	1.34	B2IV	1.34	5.7	81.2
4	NGC 4281	2006-04-17	2400	178.0	1.26	B2V	1.26	4.0	73.5
5	NGC 4472	2006-04-16	2000	155.0	1.32	B5	1.32	17.0	83.7
6	NGC 4478	2006-04-16	2400	140.0	1.39	B5V	1.39	8.5	64.5
7	NGC 4564	2006-04-16	1800	137.0	1.57	B5	1.57	5.7	89.2
8	NGC 4594	2006-04-16	1200	0.0	1.42	B5V	1.42	5.7	54.7
9	NGC 4621	2006-04-17	1200	165.0	1.33	B2IV	1.33	5.7	85.2
10	NGC 4649	2006-04-16	2000	105.0	2.27	B5III	2.27	22.7	88.7
11	NGC 4697	2006-04-16	1400	70.0	1.33	B5	1.33	8.5	85.7
12	NGC 5077	2006-04-18	3200	10.0	1.24	B8IV	1.24	6.8	75.2
13	NGC 5576	2006-04-16	1500	95.0	1.65	B2.5V	1.65	5.7	102.7
14	NGC 6909	2006-04-17	2000	70.0	1.09	B2V	1.09	2.8	52.5
Galaxies with high-resolution spectra									
15	Mrk 1055	2002-08-07	1800	179.5	1.05	G3V	1.04	2.9	78.0
16	NGC 1144	2002-08-09	1800	117.7	1.21	G3V	1.68	1.5	52.0
17	NGC 1362	2002-08-19	1800	179.5	1.02	B3V	1.23	1.5	67.0
18	NGC 4472	2002-05-19	900	179.5	1.22	B3III	1.54	5.9	71.0
19	NGC 7714	2002-07-19	1800	179.5	1.14	B3III	1.03	2.3	96.0

(1) Identification number, used in the plots, (2) Galaxy name, (3) observing Date, (4) total exposition time, (5) slit position angle, (6) airmass, (7) standard star spectral type, (8) standard star airmass, (9) length of the apertures used to extract 1-dimensional spectra shown in Figs. 2, 3 and 11, (10) average signal-to-noise per 1/pixel (see Sect. 4).

The spectra were reduced with the Image Reduction and Analysis Facility (IRAF)[1]. The sky emission was removed by either subtracting the succeeding sky image from the corresponding object image or by subtracting, from each object image, the average of the preceding and the succeeding sky images, respectively, for the two modes of observation described above. The data were flat-fielded with screen flat spectra. Geometric distortion correction was applied along both the spatial and dispersion axes by using an arc frame and the grid of stellar spectra mentioned above, respectively. Simultaneously, the frames were wavelength calibrated. We applied the dispersion corrections, and removed the hot pixels and cosmic ray hits with the algorithm described in Pych (2004). Then, we aligned the individual 2-dimensional spectra along the spatial direction (i.e. along the slit), to combine all individual spectra and extract a 1-dimensional spectrum of the galaxy for the apertures listed in Table 2.

Finally, we removed the telluric absorption. We first created a sensitivity function by multiplying the observed spectrum of the standard by the intrinsic spectrum of a star with the corresponding (or the closest available) spectral type from Pickles (1998). Some residual emission was observed, indicating that the spectral types of the standards may be inaccurate. We fitted these artificial features with a Gaussian, using the IRAF task SPLOT, and subtracted them from the sensitivity function. This prompted us to disregard the bluest part of the spectra ($\lambda \leq 1.65\,\mu$m) in further analysis because the standards were rich in hydrogen lines that modified the appearance of the galaxy spectra. We, next, divided the galaxy spectra by this sensitivity function to restore the overall continuum shape of the galaxy spectrum. This process, divided into steps, is illustrated in Fig. 1 and more detailed descriptions can be found in Hanson et al. (1996) and Maiolino et al. (1996). The final reduced spectra were corrected to zero

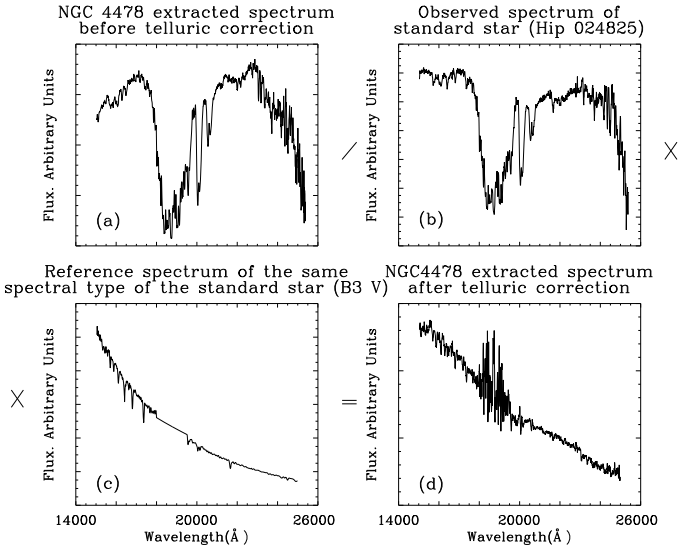

Fig. 1. The telluric absorption correction: the wavelength calibrated 1-dimensional galaxy spectrum **(a)** is divided by the wavelength calibrated 1-dimensional observed spectrum of the standard star **(b)** and the result is multiplied by the reference of the same spectral type of the standard star **(c)** from the library of Pickles (1998). The product **(d)** is the corrected galaxy spectrum. The large scatter at ~18 000–19 000 μm region is where the Earth's atmosphere is practically opaque to the radiation.

[1] Image Reduction and Analysis Facility is a general purpose software system for the reduction and analysis of astronomical data; IRAF is written and supported by the IRAF programming group at the National Optical Astronomy Observatories (NOAO).

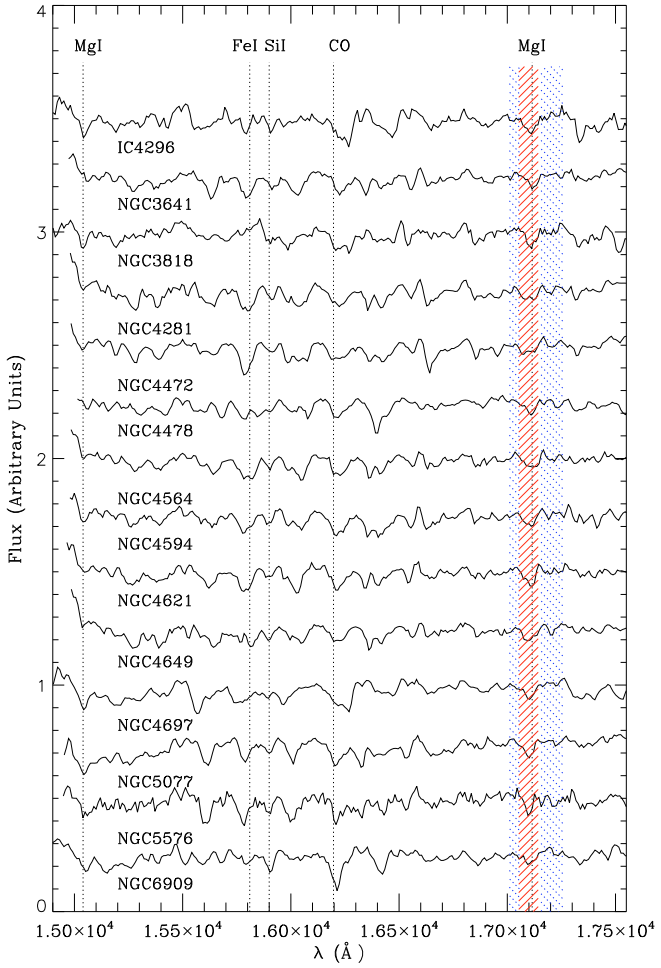

Fig. 2. *H*-band spectra of the sample galaxies, continuum-divided (i.e. all continua were normalized to 1) and shifted vertically for display purposes by adding increasing shifts of 0.25. The position of the main spectral features is shown with dotted lines. The passbands of the MgI (1.71 μm) feature and its adjacent continuum regions are marked with inclined solid and dotted lines, respectively.

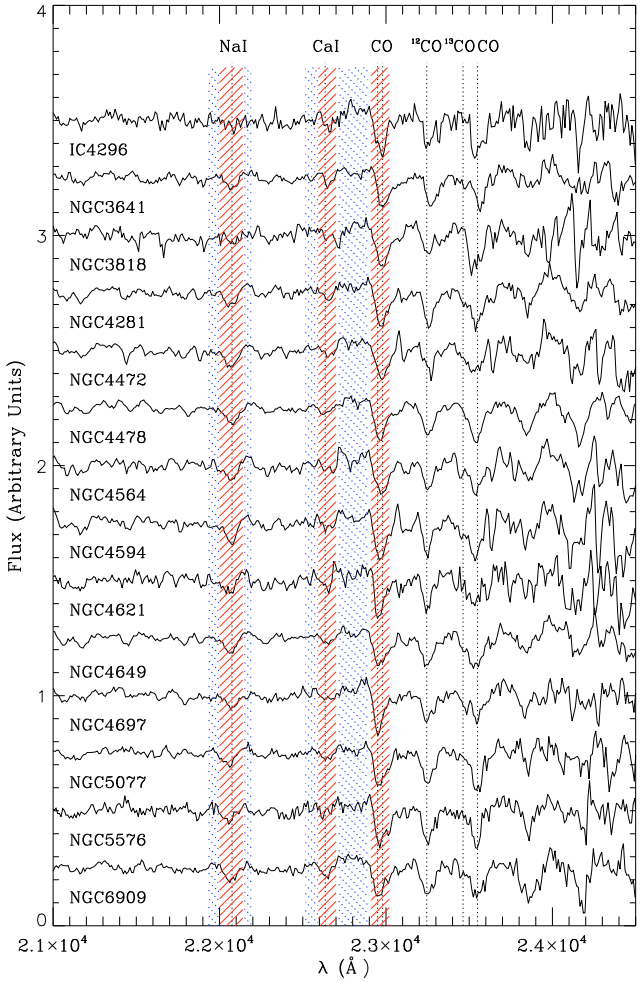

Fig. 3. *K*-band spectra of the sample galaxies, continuum-divided (i.e. all continua were normalized to 1) and shifted vertically for display purposes by adding increasing shifts of 0.25. The positions of the main spectral features are indicated by dotted lines. The passbands of the NaI (2.21 μm), CaI (2.26 μm), and CO (2.30 μm) features and their adjacent continuum regions are marked with inclined solid and dotted lines, respectively.

redshift (using values of redshift given in Table 1) and are shown in Figs. 2 and 3.

3.2. ISAAC high-resolution spectra

Five spectra of galaxies were obtained with ISAAC – a NIR imaging spectrometer (Moorwood et al. 1998a) at Nasmyth B focus of Antu, one of the 8.2-m ESO VLT unit telescopes of ESO Very Large Telescope at Paranal (Chile). It is equipped with a 1024×1024 Hawaii Rockwell HgCdTe array with a spatial scale of 0.146″ pixel^{-1}. The long-slit (0.″3×120″) medium ($R \sim 3000$) resolution spectroscopy mode was used. The wavelength coverage spans the range from ∼1.48 μm to ∼1.62 μm and the central wavelength chosen depended on the object redshift. A summary of observations is given in Table 2.

In a similar way to the SofI observations, telescope pointings ware alternated between the galaxy and a nearby clear region of sky, or if the galaxy dimensions were sufficiently small, then by nodding among two positions along the slit separated by about 20″. No jittering was used. Standards were observed in nodding mode immediately before or after the main galaxy exposure, at a similar airmass. A sequence of stellar spectra placed at equidistant positions along the slit was obtained to calibrate the spacial distortions, as in the case of the SofI data.

The reduction steps were carried out using IRAF in an identical way to that for the main data set, albeit with some complication due to the lower signal-to-noise ratio of the data and longer exposure times. First, the individual images were cleaned from cosmic rays using SPEC_COSM, a cosmic-ray rejection script for long-slit spectra developed by van Dokkum (2001). Second, bad pixels were masked out before the combination because the small number of images limited the ability of the rejection algorithms to remove the bad pixels during combination of the individual images. Finally, the highly variable sky background produced residuals in the sky-subtracted images, which were removed with the IRAF task BACKGROUND before the geometric distortion correction and the wavelength calibration.

4. Definition of the NIR spectral indices

The NIR spectral indices were usually defined with a central bandpass covering the spectral feature of interest, and two other

Table 3. NIR spectral indices.

Feature	Line		Cont. 1		Cont. 2	
	λ_c (Å)	$\Delta\lambda$ (Å)	λ_c (Å)	$\Delta\lambda$ (Å)	λ_c (Å)	$\Delta\lambda$ (Å)
MgI (1.50 μm)	15 040	80	14 960	80	15 120	80
MgI (1.71 μm)	17 098	90	17 033	46	17 206	100
NaI (2.21 μm)	22 070	140	21 965	62	22 170	40
CaI (2.26 μm)	22 647	106	22 553	74	22 802	172
CO (2.30 μm)	22 990	160	22 802	172	–	–

The central wavelength λ_c and bandwidth $\Delta\lambda$ are given for the central feature (Line) and the continuum bandpass at shorter (Cont. 1) and longer (Cont. 2) wavelengths.

bandpasses at the red and blue sides used to trace a local continuum level by a linear fit to the mean values in both bands, as in Ali et al. (1995), Frogel et al. (2001), and Ivanov et al. (2004). When this was not possible, for example because the feature was at the end of the atmospheric window, then either one continuum band or a fit to the overall shape of the continuum was used, as in Kleinmann & Hall (1986).

Most of the earlier definitions were developed for stars, where the spectral features are typically only a few km s^{-1} wide; in galaxies, however, the intrinsic velocity dispersion broadens them to a few hundred km s^{-1}. We therefore needed to define new spectral indices with broader passbands (Table 3, Figs. 2 and 3). The continuum passbands were placed in wavelength regions clear of absorption features, and not (or only weakly) affected by the telluric absorption. Furthermore, we attempted to find as wide continuum passbands as possible, to increase the signal-to-noise ratio of the index measurements. The passband of each spectral feature was defined to encompass the maximum extent of the feature itself and avoid, if possible, contamination by other features. For instance, the passband of our CO (2.30 μm) index is wide but still only includes the ^{12}CO feature and no contribution from the ^{13}CO band head.

We measured the equivalent width (*EW*) of the lines with respect to a local continuum obtained by fitting a straight line to the "clear" parts of the spectrum:

$$EW = (1 - F_{\rm feature}/F_{\rm cont}) * \Delta\lambda \quad (1)$$

where $F_{\rm feature}$ is the flux inside the feature window, $F_{\rm cont}$ is the value of the local continuum linearly interpolated (or extrapolated, if necessary) to the center of the line, and $\Delta\lambda$ is the width of the feature bandpass. The fluxes $F_{\rm feature}$ and $F_{\rm cont}$ were normalized by the bandpass widths. The measurements were performed following the above recipe with a specially developed IDL script. The error bars of the measurements were derived by the same script by means of Monte Carlo simulations on the measured spectrum considering as noise the rms of the normalized flux in the continuum region. The average signal-to-noise ratio calculated in the continuum passbands region is written in Table 2. The corresponding values of each equivalent width with their relative errors for all galaxies in the sample are given in Table 4.

Our definitions have intentionally wide bandpasses to ensure that they are quite insensitive to the varying velocity broadening of spectral features in the galaxy spectra. To verify this, we measured the indices for broadened spectra of M and K type giants. We chose stars in this spectral range because they are the most representative of early-type galaxy integrated light spectra.

Table 4. Equivalent widths of the newly defined NIR spectral indices for the sample galaxies.

Galaxy	MgI $EW \pm\sigma(EW)$ (Å)	NaI $EW\pm\sigma(EW)$ (Å)	CaI $EW\pm\sigma(EW)$ (Å)	CO $EW\pm\sigma(EW)$ (Å)
IC 4296	2.44 ± 0.40	5.74 ± 0.37	4.01 ± 0.35	15.48 ± 0.63
NGC 3641	2.54 ± 0.43	4.48 ± 0.40	1.88 ± 0.56	14.28 ± 0.57
NGC 3818	3.23 ± 0.20	5.64 ± 0.19	2.67 ± 0.53	13.63 ± 0.65
NGC 4281	3.07 ± 0.26	3.35 ± 0.28	3.08 ± 0.59	16.00 ± 0.80
NGC 4472	3.04 ± 0.44	6.11 ± 0.18	2.72 ± 0.17	14.01 ± 0.63
NGC 4478	3.50 ± 0.29	4.45 ± 0.43	1.91 ± 0.81	14.29 ± 1.00
NGC 4564	2.97 ± 0.36	6.69 ± 0.15	2.25 ± 0.41	14.84 ± 0.71
NGC 4594	3.24 ± 0.39	7.35 ± 0.35	3.01 ± 0.40	14.65 ± 1.12
NGC 4621	2.73 ± 0.23	6.25 ± 0.11	2.79 ± 0.28	15.09 ± 0.64
NGC 4649	2.77 ± 0.40	6.49 ± 0.16	3.10 ± 0.25	14.19 ± 0.60
NGC 4697	3.14 ± 0.41	5.85 ± 0.20	3.10 ± 0.28	14.88 ± 0.58
NGC 5077	3.72 ± 0.56	1.90 ± 0.15	2.78 ± 0.84	14.64 ± 1.06
NGC 5576	2.37 ± 0.30	4.27 ± 0.15	1.75 ± 0.41	12.63 ± 0.70
NGC 6909	3.60 ± 0.48	2.59 ± 0.46	2.72 ± 0.77	15.22 ± 0.94

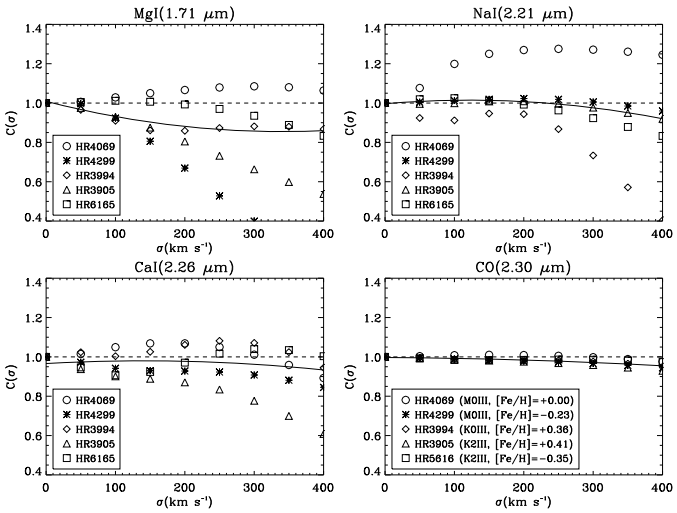

Fig. 4. Correction factors of the NIR spectral index for different values of velocity dispersion. They were derived by comparing the *EW* measured in the spectra of the labeled stars before and after broadening them to a particular velocity dispersion. The spectral types of the stars are in a range between KIII and MIII with a spread of [Fe/H] between −0.35 and +0.41. In each panel, the solid line is the 2nd order polynomial fitting the data.

(These spectra are a reasonable match to the observed galaxy spectra.) We computed for them the correction factor $C(\sigma)$ for various line-of-sight velocity distribution, as in S08:

$$C(\sigma) = \frac{EW(\sigma = 0)}{EW(\sigma)} \cdot \quad (2)$$

The *EW* of the feature was measured from the stars convolved with a Gaussian of width σ given in brackets. We broadened the stellar spectra to a velocity dispersion of up to 400 km s^{-1} in steps of 50 km s^{-1} and used templates for different spectral stars and from different sources. The corrections for the different spectral indices are shown in Fig. 4; some exhibit significant scatter, depending on the adopted stellar spectrum. However, the mean correction was typically small (i.e. $\lesssim$15% at its most extreme).

5. Discussion and conclusions

5.1. General appearance of the spectra

The spectra of our sample galaxies appear qualitatively similar in most of the NIR features except for a large spread in the NaI values. This similarity is unsurprising because we selected mostly giant ellipticals and spheroids, which are all relatively metal rich, have no significant recent star formation, and only weak nuclear activity, if any. This conclusion agrees with Mannucci et al. (2001), who demonstrated that galaxies of the same Hubble type have almost identical NIR spectra. On the other hand, the large spread in NaI, with respect to the observational errors, appears to be real, and suggests that a variety of star formation and enrichment histories exist among the galaxies in our sample. Two of the three galaxies with systematically weaker NaI exhibit strong Hβ, indicating that the weak NaI might be related to the presence of younger stellar populations (the third galaxy lacks optical spectroscopy). The strongest features are the CO absorption bands in both the H and K-band atmospheric windows. They originate in K and M stars, as can be seen from the libraries of stellar spectra described by Lancon & Rocca-Volmerange (1992), Origlia et al. (1993), Dallier et al. (1996), Meyer et al. (1998), Wallace & Hinkle (1997), and Förster Schreiber (2000). A number of weaker metal absorption features are visible as well: SiI at 1.589 μm, MgI at 1.711 μm, NaI at 2.206 and 2.209 μm, and CaI at 2.261, 2.263, and 2.266 μm. These are also present mostly in cool stars (i.e. Kleinmann & Hall 1986; Origlia et al. 1993; Wallace & Hinkle 1997; Förster Schreiber 2000; Meyer et al. 1998). As mentioned above, we only consider the redder features with $\lambda \geq 1.65$ μm.

Unsurprisingly, our galaxies show no FeII at 1.644 μm or H_2 lines line emission, usually associated with supernova activity and supernova related shocks, respectively. There is also no Brγ emission.

5.2. Behavior of the NIR spectral indices

Evolutionary synthesis models (i.e. Worthey 1994) are the usual method to interpret the behavior of spectral features in galaxies, but the simple comparison of these features with the galaxy parameters can be informative too. For example, the optical indices, Mg_2 , $\langle$Fe$\rangle$, and H_β show tight correlations with the central velocity dispersion (e.g. Terlevich et al. 1981; Bernardi et al. 1998; Mehlert et al. 2003; Morelli et al. 2008), suggesting that the chemical and dynamical evolution of ellipticals are intertwined.

The *EW* of our NIR spectral indices, the iron abundance, and metallicity are plotted versus the central velocity dispersion in Fig. 5. The loci of the S08 data (see their Fig. 13) are shown with dashed lines. Among the galaxies, NGC 5077 (#12) and NGC 6909 (#14) possess very weak NaI, CaI lines, and their relative errors are significant. The correlations between the NIR indices and velocity dispersion for the sample galaxies are plotted in Fig. 5; the fit do not consider NGC 4281 (#4), NGC 5077 (#12), and NGC 6909 (#14) because of the reasons explained further on. The correlation with CO shows a similar slope to that found by S08 but with a different zero-point. The difference in the index definition and especially the position of the continuum bandpass can produce systematic variation of the *EW* values. This effect seems to be more evident in the CO band, whose equivalent width is measured using only an extrapolated continuum blue-wards of the feature. The agreement with S08 is closer for the NaI versus σ relation, although our data show larger scatter. Without derive a general conclusion, we found relatively high NaI values compared with stars, similar was also found by S08. The iron abundance [Fe/H] and total abundance [Z/H] were only weakly correlated. Active galaxies were clustered towards the high end of the velocity dispersion distribution, which is understandable because their velocity dispersion measurement may be affected by the presence of a black hole and active nucleus. We note that our highest velocity dispersion galaxy is a type 2 Seyfert and the CO band may suffer some dilution, as discussed by Ivanov et al. (2000).

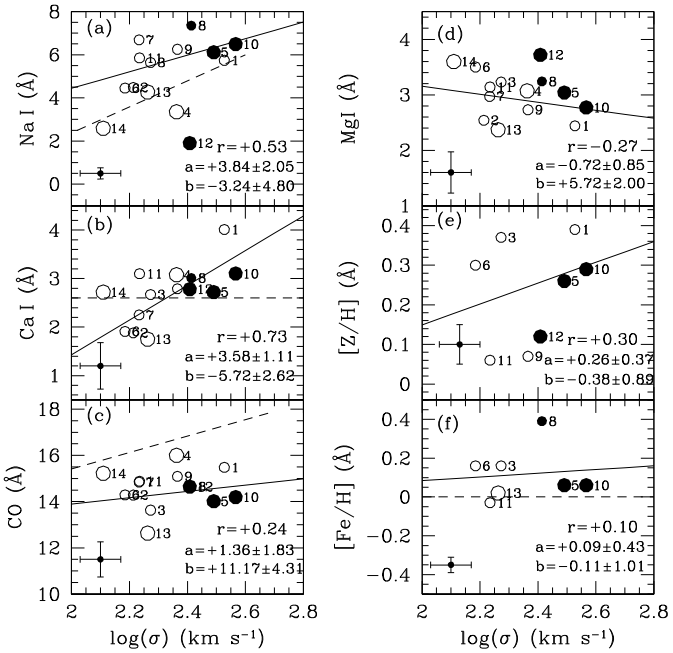

Fig. 5. The equivalent widths of the NIR spectral indices, iron abundance [Fe/H], and metal abundance [Z/H] in the sample galaxies as a function of the central velocity dispersion. The labels correspond to the row numbers in Table 1. The open and filled circles refer to quiescent and active galaxies, respectively. The small and large circles represent galaxies with an age of between 5 and 10 Gyr and >10 Gyr, respectively. Galaxies with no known ages were assumed to be old. The dashed lines corresponds to the relations found by S08. The solid line in each panel represents the best fit linear regression ($y = ax+b$) for all the data points except for #4, #12 and #14. The Pearson correlation coefficient (r) and the results of the linear fit are given. Typical error bars are shown.

The *EW*s of our NIR spectral indices are plotted versus each other in Fig. 6 and compared with the relations for cluster stars and solar neighborhood giants by S08 and Davidge et al. (2008), respectively. Three galaxies – NGC 4281 (#4), NGC 5077 (#12) and NGC 6909 (#14) – are above the relation of S08 for cluster stars, which suggests that they may have different chemical enrichment histories with respect to the remainder of the sample. Unfortunately the literature lacks data about these objects and although NGC 6909 is of the lowest velocity dispersion in our sample, these galaxies do not appear to be extremely distinctive in any respect, including in the terms of optical Mg_2 versus σ diagram. Further investigation of these galaxies is necessary. The remaining galaxies populate a locus that follows similar trends to the galaxies of S08. In the CaI versus CO plot we see a correlation with significant scatter, and with a different slope than in S08. Finally, the MgI versus CO plot is dominated by scatter. Galaxies with traces of nuclear activity, evident in other wavelength ranges than the NIR, do not appear to differ from the remainder of the sample, and show no emission lines. Therefore,

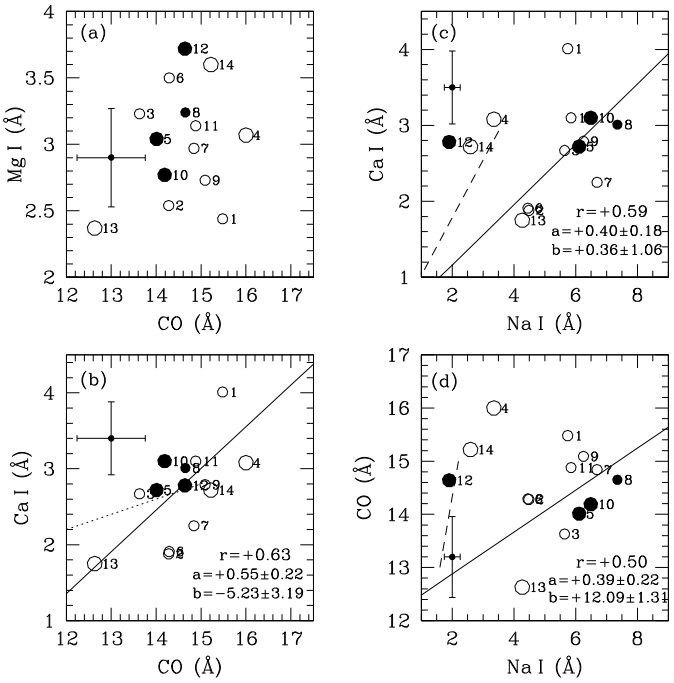

Fig. 6. The equivalent widths of the NIR indices plotted against each other. The symbols are the same as in Fig. 5. The dashed lines correspond to the relations found by S08. The dotted line corresponds to the relation by Davidge et al. (2008) for giant stars in the solar neighborhood. All of these relations are plotted in their observed range. The solid line represents the linear regression ($y = ax + b$) through all data points except for #4, #12, and #14. The Pearson correlation coefficient (r) and the results of the linear fit are given. Typical error bars are shown.

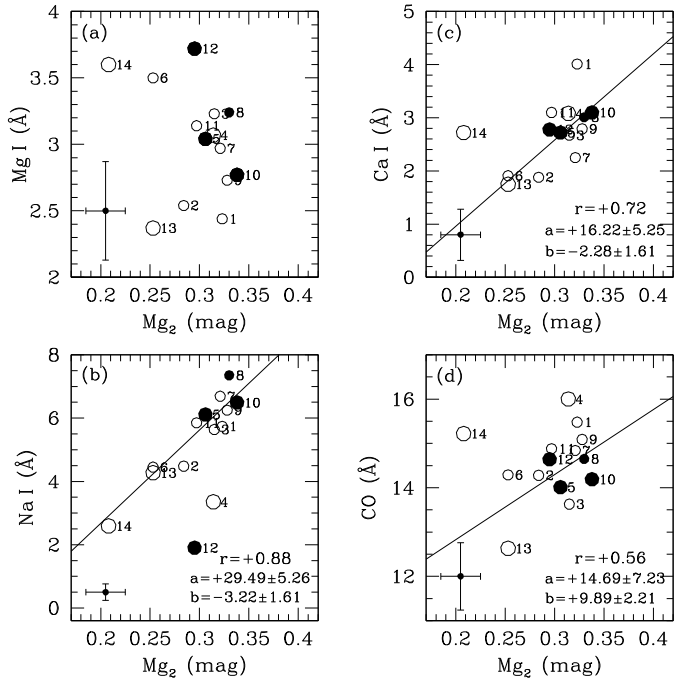

Fig. 7. The equivalent widths of the NIR indices plotted against the Mg$_2$ indices measured by Bender et al. (1993). The symbols are the same as in Fig. 5. The solid line represents the linear regression ($y = ax + b$) through all data points except for #4, #12, and #14. The Pearson correlation coefficient (r) and the results of the linear fit are given. Typical error bars are shown.

the contribution of their AGNs to their detected spectrum is negligible compared with that of the remainder of the galaxy.

Figure 7 shows the *EW* of the NIR spectral indices versus the Mg$_2$ measurements from Bender et al. (1993). NaI, and to a lesser extent CaI and CO, show trends with respect to Mg$_2$, with NGC 4281 (#4), NGC 5077 (#12), and NGC 6909 (#14) standing out. The correlation of NaI with both σ and Mg$_2$ suggests that the NaI feature is dominated by the stellar photosphere rather than the interstellar medium.

Given that [Fe/H] measurements are unavailable for the entire sample and Mg$_2$ is unrepresentative of the total chemical abundance of a galaxy because of the varying abundance ratios, we attempted to create a combined Iron-and-α-element index similar to that defined by González (1993) and more recently by Thomas et al. (2003):

$$[\mathrm{MgFe}]' = \sqrt{\mathrm{Mg}b \times (0.72 \times \mathrm{Fe5270} + 0.28 \times \mathrm{Fe5335})}. \quad (3)$$

Such a combined indicator is expected to decrease the effect of variation in the α/Fe ratio. Since not all input parameters of this indicator are available, we substitute directly in the iron and magnesium indices by defining a new indicator:

$$[\mathrm{MgFe}]'' = \sqrt{\mathrm{Mg}_2 \times \mathrm{Fe5335}}. \quad (4)$$

The results are shown in Figs. 8a–c. The NaI index of NGC 5077 (#12) and the CO index of NGC 6909 (#14) deviate from the main loci of the other galaxies.

To address this issue, we plotted the optical indices of these galaxies versus the combined [MgFe]″ index (Fig. 8d). This is an analog of the typical plot (i.e. Worthey 1994) that allows us to disentangle the age-metallicity degeneracy: the inverse H$_\beta$ index

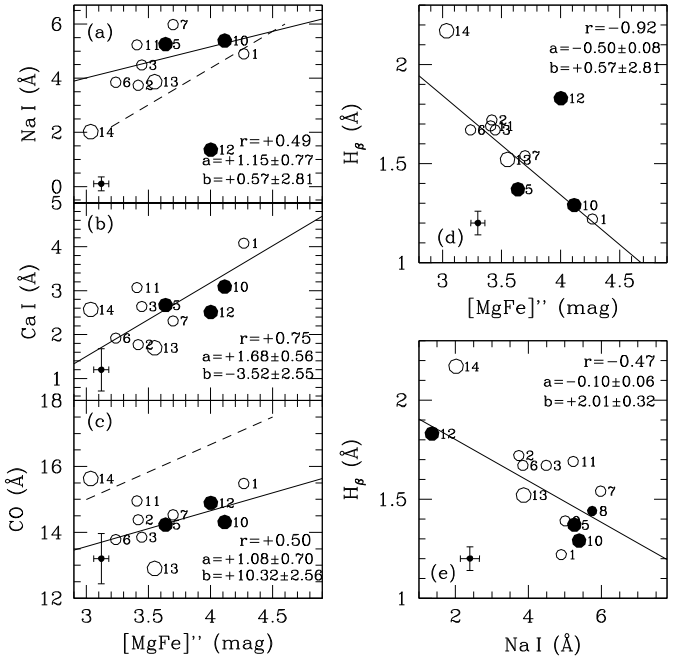

Fig. 8. a–d) The equivalent widths of the NaI, CaI, CO and Hβ indices plotted against the [MgFe]″ index. **e)** The equivalent widths of the Hβ index as a function of the NaI index. The symbols are the same as in Fig. 5. The dashed lines correspond to the relations found by S08. The solid line represents the linear regression ($y = ax + b$) through all data points except for #4, #12, and #14. The Pearson correlation coefficient (r) and the results of the linear fit are given. Typical error bars are shown.

is approximately proportional to age, while the [MgFe]″ is dominated by metal abundance. The two galaxies exhibit strong H$_\beta$,

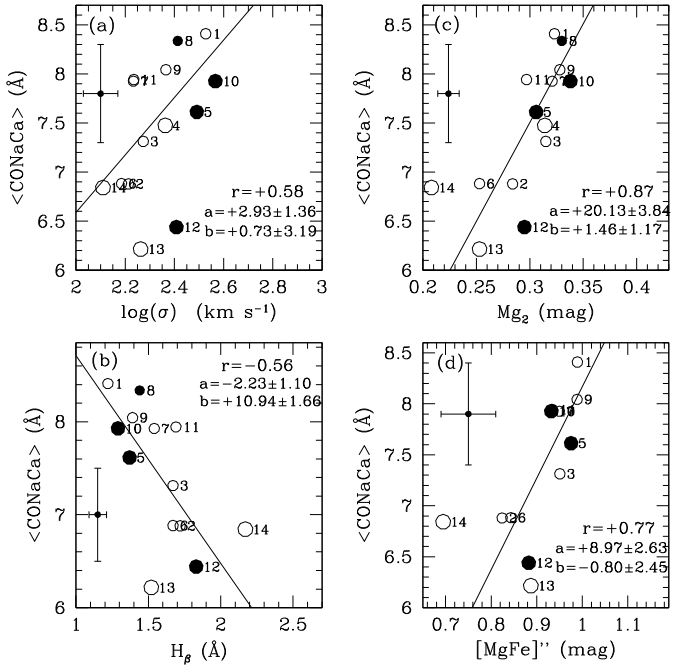

Fig. 9. The equivalent widths of the newly defined ⟨CONaCa⟩ as a function of the central velocity dispersion **a)**, Mg_2 **b)**, Hβ **c)**, and [FeMg]$''$ **d)** indices. The symbols are the same as in Fig. 5. The solid line represents the linear regression ($y = ax + b$) through all the data points except for #4, #12 and #14. The Pearson correlation coefficient (r) and the results of the linear fit are given. Typical error bars are shown.

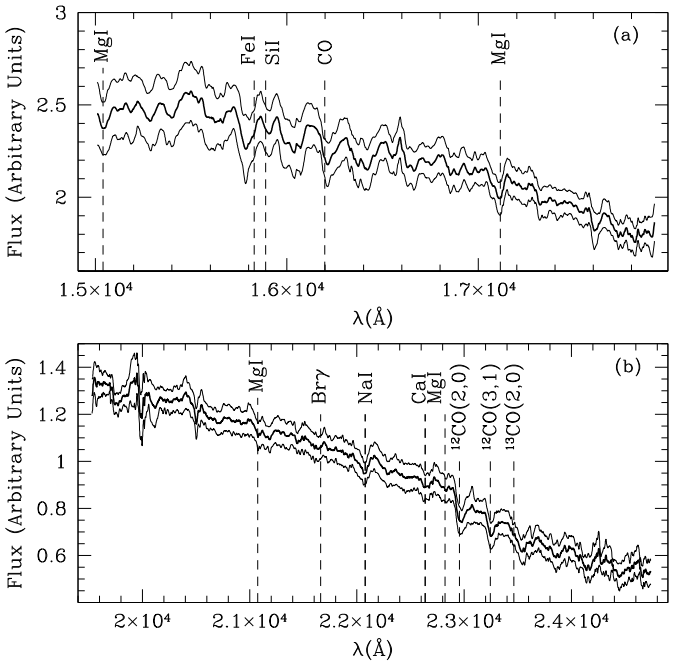

Fig. 10. Average H- **a)** and K-band **b)** spectrum of sample galaxies normalized to unity at 22 000 Å (thick line). The thin lines correspond to the $\pm 1\sigma$ confidence levels. Some of the more prominent spectral features are indicated.

which suggests that they are dominated by populations of 3 Gyr or younger (see for example Fig. 1 in S08). NGC 5077 and NGC 6909 are also well separated from the remainder of the galaxies in the H$_\beta$ versus NaI plot (Fig. 8e); this leads us to the conclude that the NIR indices can be used to create a similar diagnostic plot, but measuring the Brγ feature requires higher quality data than presented here.

We investigated the behavior of the NIR indices with respect to the H and K-band magnitude and $H - K$ color, but no clear correlations were found.

5.3. Combined NIR metal index

Ground-based NIR spectroscopic observations are far more time consuming to acquire than the corresponding optical observations – higher and variable background and detectors with poorer cosmetics often require one to sacrifice either resolution or signal-to-noise ratio to obtain the data in a reasonable amount of time. To alleviate this problem, we defined a combined spectral index of all the major K-band metal features:

$$\langle \mathrm{CONaCa} \rangle = (\mathrm{CO} + \mathrm{Na\,I} + \mathrm{Ca\,I})/3.0. \quad (5)$$

Various weighting schemes were attempted to minimize the scatter of the basic relations. However, the simple average yielded the tightest relations (Fig. 9). The carbon and oxygen are α elements, while the sodium and calcium originate in both high and low mass stars. The average value of the CO index for the sample galaxies was ∼15 Å, of NaI was ∼4.3 Å and of CaI was ∼2.7 Å, which implies that at least 2/3 of the *EW* of the new index is dominated by metals produced mostly in high mass stars, i.e. early in the star formation history of the elliptical galaxies. The other implication is that a relatively limited amount of recent star formation could affect the new index more than it would an iron-peak-dominated index. The lack of iron peak features in the NIR is well known as pointed out in Ivanov (2001).

The new index improves the tightness of the correlations. For example, the Pearson correlation coefficient is ∼10% higher for the ⟨CONaCa⟩ versus Mg2 relation and ∼20% higher for the ⟨CONaCa⟩ versus [MgFe]$''$ relation, with respect to the respective correlations in which only one IR index is used. We derived these relations using only galaxies with known parameters, i.e. excluding the poorly studied NGC 4281(#4), NGC 5077(#12) and NGC 6909(#14) which show systematic peculiarities with respect to the bulk of our sample.

5.4. Average NIR spectrum of the sample galaxies

Studies of composite stellar systems (i.e. galaxies hosting an AGN) often need to subtract the contribution of the underlying galaxy. This prompted us to create an average spectrum of the galaxies in our sample. We used a homogeneous subset of eight galaxies, excluding the objects with young populations. We also excluded those with spectra of low signal-to-noise ratio. The average age of the galaxies used to create the composite spectrum was 9 ± 2 Gyr (the median was 9.5 Gyr) and the average [Fe/H] was 0.17 ± 0.13 (the median was 0.16). The composite spectrum is shown in Fig. 10 and the measurements completed for the spectrum are listed in Table 5, including r.m.s. values per Angstrom. We included the H-band section because the artifacts caused by the spectral-type mismatch of the standards are minimized by the averaging of galaxies observed at different redshifts.

5.5. The MgI feature at 1.51 μm

Ivanov et al. (2004) pointed out the possibility of using the MgI feature at 1.51 μm as an α-element abundance indicator in the NIR. For exploratory purposes, we obtained spectra of a

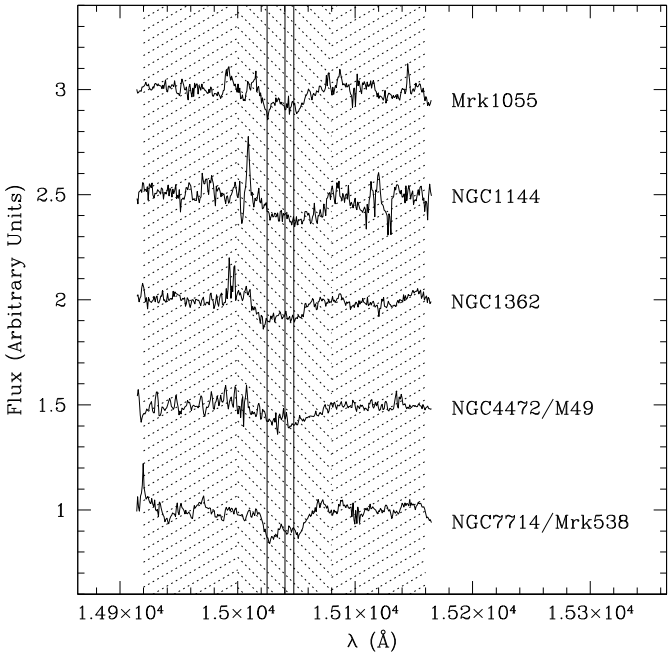

Fig. 11. Spectra of the galaxies observed with ISAAC in the region of the MgI (1.51 μm). The central wavelengths of the individual MgI lines are shown with vertical solid lines. The passbands for the feature and the adjacent continua are shaded. The spectra were normalized to unity and shifted vertically by 0.5 for display purposes.

Table 5. Average spectrum of the sample galaxies observed at NTT in arbitrary units and normalized to unity at 22 000 Å. The regions with zero rms at the beginning and the end are covered only by one or two spectra. The full table is only available in the electronic version at the CDS.

λ (Å)	F_λ	rms
14944	2.217	0.000
14945	2.384	0.000
14946	2.384	0.000
14947	2.386	0.000
14948	2.130	0.366
14949	2.572	0.254
14950	2.575	0.251
14951	2.578	0.248
14952	2.583	0.245
14953	2.588	0.243
14954	2.595	0.241
14955	2.602	0.240

small and diverse set of galaxies (Table 2 and Fig. 11). To carry out a quantitative analysis, we defined an index (Table 3), and for five galaxies, we measured its equivalent width to be 3.3, 5.0, 3.8, 3.9, and 4.5 Å, respectively, for Mrk 1055, NGC 1144, NGC 1362, NGC 4472, and NGC 7714. The typical uncertainty was ~0.3 Å. No corrections for velocity dispersion were applied. Given the diverse nature of these objects, we refrain from drawing any conclusions, but we note that the relation between the optical and NIR Mg features is not straightforward because the only two Mg_2 values present in the literature are inversely proportional to our index measurements for NGC 1362 and NGC 4472. Nevertheless, these observations prove that it is feasible to measure the NIR MgI feature at 1.51 μm and provide a basis for future NIR synthetic spectral modeling.

6. Summary

We have presented a new data set of NIR spectra of ellipticals/spheroids to provide independent constraints on the properties of their stellar populations. They cover a wide range in luminosity and velocity dispersion, and have available Lick/IDS line-strength indices from literature.

1. The stronger features were measured and showed mild correlations with the optical metal features. NIR versus NIR features showed significant scatter but the diagram of CO versus NaI appears to be a good diagnostic for detecting different chemical enrichment histories.
2. The NIR metal absorption, in combination with a hydrogen absorption feature may be able to break the age-metallicity degeneracy, but further investigation and higher quality data are required to verify this possibility.
3. A new combined NIR index was defined that allows one to interpret lower signal-to-noise data. It is dominated, at about the 2/3 level, by α-elements. We also present an average spectrum of ellipticals/spheroids, constructed from a homogeneous subset of our sample that can be used as a template integrated early-type galaxy spectrum.
4. The strength of MgI feature at 1.5 μm was measured for the first time in a heterogeneous sample of galaxies, providing a new constraint for future NIR spectral synthesis models.

Acknowledgements. We thank Reynier Peletier for useful discussion and suggestions. We acknowledge grant CPDA068415/06 by Padua University, which provided support for this research. M.C. thanks the European Southern Observatory for support via ESO Studentship program. L.M. is supported by grant (CPDR061795/06) by Padova University. L.M. acknowledge the Pontificia Universidad Catolica de Chile and the European Southern Observatory for hospitality while this paper was in progress. We are grateful to the La Silla and Paranal staff astronomers for their support.

References

Ali, B., Carr, J. S., Depoy, D. L., Frogel, J. A., & Sellgren, K. 1995, AJ, 110, 2415
Alonso-Herrero, A., Rieke, M. J., Rieke, G. H., & Shields, J. C. 2000, ApJ, 530, 688
Annibali, F., Bressan, A., Rampazzo, R., Zeilinger, W. W., & Danese, L. 2007, A&A, 463, 455
Bender, R., Burstein, D., & Faber, S. M. 1993, ApJ, 411, 153
Bernardi, M., Renzini, A., da Costa, L. N., et al. 1998, ApJ, 508, L143
Bernardi, M., Alonso, M. V., da Costa, L. N., et al. 2002, AJ, 123, 2990
Binggeli, B., Sandage, A., & Tammann, G. A. 1985, AJ, 90, 1681
Boisson, C., Coupé, S., Cuby, J. G., Joly, M., & Ward, M. J. 2002, A&A, 396, 489
Burstein, D., Faber, S. M., Gaskell, C. M., & Krumm, N. 1984, ApJ, 287, 586
Burston, A. J., Ward, M. J., & Davies, R. I. 2001, MNRAS, 326, 403
Cenarro, A. J., Gorgas, J., Vazdekis, A., Cardiel, N., & Peletier, R. F. 2003, MNRAS, 339, L12
Coziol, R., Doyon, R., & Demers, S. 2001, MNRAS, 325, 1081
Cutri, R. M., Skrutskie, M. F., van Dyk, S., et al. 2003, 2MASS All Sky Catalog of point sources, The IRSA 2MASS All-Sky Point Source Catalog, NASA/IPAC Infrared Science Archive, http://irsa.ipac.caltech.edu/applications/Gator/
da Costa, L. N., Willmer, C. N. A., Pellegrini, P. S., et al. 1998, AJ, 116, 1
Dalle Ore, C., Faber, S. M., Jesus, J., Stoughton, R., & Burstein, D. 1991, ApJ, 366, 38
Dallier, R., Boisson, C., & Joly, M. 1996, A&AS, 116, 239
Das, M., & Jog, C. J. 1999, ApJ, 527, 600
Davidge, T. J., Beck, T. L., & McGregor, P. J. 2008, ApJ, 677, 238
de Vaucouleurs, G., de Vaucouleurs, A., Corwin, Jr., H. G., et al. 1991, Third Reference Catalogue of Bright Galaxies (Berlin: Springer-Verlag)

Denicoló, G., Terlevich, R., Terlevich, E., et al. 2005, MNRAS, 356, 1440
Devillard, N. 1999, in Astronomical Data Analysis Software and Systems VIII, ed. D. M. Mehringer, R. L. Plante, & D. A. Roberts, ASP Conf. Ser., 172, 333
Engelbracht, C. W. 1997, Ph .D. Thesis, Univ. of Arizona
Faber, S. M. 1973, ApJ, 179, 731
Faber, S. M., Friel, E. D., Burstein, D., & Gaskell, C. M. 1985, ApJS, 57, 711
Faber, S. M., Trager, S. C., Gonzalez, J. J., & Worthey, G. 1999, Ap&SS, 267, 273
Falco, E. E., Kurtz, M. J., Geller, M. J., et al. 1999, PASP, 111, 438
Förster Schreiber, N. M. 2000, AJ, 120, 2089
Frogel, J. A., Stephens, A., Ramírez, S., & DePoy, D. L. 2001, AJ, 122, 1896
Gardner, J. P., Mather, J. C., Clampin, M., et al. 2006, Space Sci. Rev., 123, 485
Goldader, J. D., Joseph, R. D., Doyon, R., & Sanders, D. B. 1995, ApJ, 444, 97
Goldader, J. D., Joseph, R. D., Doyon, R., & Sanders, D. B. 1997, ApJS, 108, 449
González, J. J. 1993, Ph. D. Thesis, Univ. of Califonia, Santa Cruz
Hanson, M. M., Conti, P. S., & Rieke, M. J. 1996, ApJS, 107, 281
Heckman, T. M. 1980, A&A, 87, 152
Ho, L. C., Filippenko, A. V., & Sargent, W. L. W. 1997, ApJS, 112, 315
Howell, J. H. 2005, AJ, 130, 2065
Ivanov, V. D. 2001, Ph. D. Thesis, Univ. of Arizona
Ivanov, V. D., Rieke, G. H., Groppi, C. E., et al. 2000, ApJ, 545, 190
Ivanov, V. D., Rieke, M. J., Engelbracht, C. W., et al. 2004, ApJS, 151, 387
Keel, W. C. 1996, ApJS, 106, 27
Kleinmann, S. G., & Hall, D. N. B. 1986, ApJS, 62, 501
Kobayashi, C., & Arimoto, N. 1999, ApJ, 527, 573
Lancon, A., & Rocca-Volmerange, B. 1992, A&AS, 96, 593
Larkin, J. E., Armus, L., Knop, R. A., Soifer, B. T., & Matthews, K. 1998, ApJS, 114, 59
Lauberts, A., & Valentijn, E. A. 1989, The Messenger, 56, 31
Lu, N. Y., Hoffman, G. L., Groff, T., Roos, T., & Lamphier, C. 1993, ApJS, 88, 383
Maiolino, R., Rieke, G. H., & Rieke, M. J. 1996, AJ, 111, 537
Mannucci, F., Basile, F., Poggianti, B. M., et al. 2001, MNRAS, 326, 745
Mehlert, D., Thomas, D., Saglia, R. P., Bender, R., & Wegner, G. 2003, A&A, 407, 423
Meyer, M. R., Edwards, S., Hinkle, K. H., & Strom, S. E. 1998, ApJ, 508, 397
Moorwood, A., Cuby, J.-G., Biereichel, P., et al. 1998a, The Messenger, 94, 7
Moorwood, A., Cuby, J.-G., & Lidman, C. 1998b, The Messenger, 91, 9
Morelli, L., Pompei, E., Pizzella, A., et al. 2008, MNRAS, in press [arXiv:0806.2988]
Murphy, Jr., T. W., Soifer, B. T., Matthews, K., Kiger, J. R., & Armus, L. 1999, ApJ, 525, L85
Murphy, Jr., T. W., Soifer, B. T., Matthews, K., Armus, L., & Kiger, J. R. 2001, AJ, 121, 97
O'Connell, R. W. 1986, PASP, 98, 163
Ogando, R. L. C., Maia, M. A. G., Pellegrini, P. S., & da Costa, L. N. 2008, AJ, 135, 2424
Oliva, E., Origlia, L., Kotilainen, J. K., & Moorwood, A. F. M. 1995, A&A, 301, 55
Origlia, L., Moorwood, A. F. M., & Oliva, E. 1993, A&A, 280, 536
Pickles, A. J. 1998, PASP, 110, 863
Pych, W. 2004, PASP, 116, 148
Rampazzo, R., Annibali, F., Bressan, A., et al. 2005, A&A, 433, 497
Reunanen, J., Kotilainen, J. K., & Prieto, M. A. 2002, MNRAS, 331, 154
Reunanen, J., Tacconi-Garman, L. E., & Ivanov, V. D. 2007, MNRAS, 382, 951
Rinn, A. S., Sambruna, R. M., & Gliozzi, M. 2005, ApJ, 621, 167
Sánchez-Blázquez, P., Forbes, D. A., Strader, J., Brodie, J., & Proctor, R. 2007, MNRAS, 377, 759
Silva, D. R., Kuntschner, H., & Lyubenova, M. 2008, ApJ, 674, 194
Smith, R. J., Lucey, J. R., Hudson, M. J., Schlegel, D. J., & Davies, R. L. 2000, MNRAS, 313, 469
Sosa-Brito, R. M., Tacconi-Garman, L. E., Lehnert, M. D., & Gallimore, J. F. 2001, ApJS, 136, 61
Stephens, A. W., & Frogel, J. A. 2004, AJ, 127, 925
Terlevich, R., Davies, R. L., Faber, S. M., & Burstein, D. 1981, MNRAS, 196, 381
Thomas, D., Maraston, C., & Bender, R. 2003, MNRAS, 339, 897
Trager, S. C., Worthey, G., Faber, S. M., Burstein, D., & Gonzalez, J. J. 1998, ApJS, 116, 1
Trager, S. C., Faber, S. M., Worthey, G., & González, J. J. 2000, AJ, 120, 165
Trager, S. C., Worthey, G., Faber, S. M., & Dressler, A. 2005, MNRAS, 362, 2
van Dokkum, P. G. 2001, PASP, 113, 1420
Vanzi, L., & Rieke, G. H. 1997, ApJ, 479, 694
Vanzi, L., Alonso-Herrero, A., & Rieke, G. H. 1998, ApJ, 504, 93
Wallace, L., & Hinkle, K. 1997, ApJS, 111, 445
Wegner, G., Bernardi, M., Willmer, C. N. A., et al. 2003, AJ, 126, 2268
Worthey, G. 1994, ApJS, 95, 107